PERGAMON

International Journal of Multiphase Flow 27 (2001) 527–551

International Journal of Multiphase Flow

www.elsevier.com/locate/ijmulflow

A study of bubbling and slugging fluidised beds using the two-fluid granular temperature model

C.C. Pain*, S. Mansoorzadeh, C.R.E. de Oliveira

Computational Physics and Geophysics Group, T H Huxley School of Environment, Earth Sciences and Engineering, Imperial College of Science, Technology and Medicine, London SW7 2BP, UK

Received 15 March 1999; received in revised form 12 April 2000

Abstract

This paper reports finite element numerical simulations of gas–solid fluidised beds using the two-fluid granular temperature model. The aim of the study has been to investigate the various phenomena that have been observed in fluidised beds but have not been subject to numerical investigation. Two fluidised beds, operating in the slugging and bubbling regimes, were modelled, and the formation, elongation, coalescence and eruption of bubbles described. The effect of an obstruction on the fluidisation efficiency in a fluidised bed was investigated. Granular temperature distribution inside the fluidised bed provided an indication of the regions on the obstruction, which could be susceptible to erosion by particle impact.

Keywords: Fluidised bed; Finite element method; Two-fluid model; Granular temperature

1. Introduction

Understanding the dynamics of fluidised beds is a key issue in making improvements in efficiency of fluidisation. Perforce, this understanding will have to be achieved through numerical modelling as experimental data, though essential, will not be able to provide the necessary comprehensive description of fluidised bed behaviour. The rapid development of

* Corresponding author.
E-mail address: c.pain@ic.ac.uk (C.C. Pain).

0301-9322/01/$ - see front matter
PII: S0301-9322(00)00035-5

computers, numerical methods and solution techniques are now beginning to provide the tools necessary to model the dynamics of these complex systems.

Numerical approaches used in the literature for modelling particle–fluid flow can be divided into two categories: continuum and discrete models. Continuum models assume that the dispersed phase behaves as a fluid. Discrete modelling, on the other hand, deals with individual particles. This fundamental modelling approach, used for example by Tsuji and Kawaguchi (1993), involves the interaction between individual particles subjected to drag forces exerted by the fluidising gases. To simulate inter-particle collisions, two models are used: the hard sphere model and the soft sphere model (Tsuji and Kawaguchi, 1993; Crowe et al., 1998). Impulse equations, together with the restitution coefficient, relate the velocities of particles before and after collision. In the soft sphere model, forces acting on particles during contact are also considered. This approach involves modelling, explicitly, granular turbulence, and has the advantages of simplicity and that the characteristic properties of individual particles such as size and density can be specified. The ability to model the rotation and velocity of individual particles is another advantage of this method. The main limitations are that it needs small time steps to model the contact between particles and that each particle in the system needs to be modelled.

The two-fluid model (TFM) is perhaps the most commonly used model for predicting the dynamical behaviour of fluid–particle systems (see, for example, Soo, 1967; Enwald et al., 1996, and references therein). In this model, the gas and particulate phases are assumed to form two inter-penetrating continua, and continuity, momentum and energy equations are written for both, the particulate and fluid phases. In the work of Gera et al. (1998), the results for simulations of single bubble formation using a TFM and an individual particle tracking model were compared which showed agreement, further supporting the case for the use of the former approach. The formation of a single bubble has also been simulated using other numerical models. Harris (1996), for example, used a numerical method to calculate the velocity potential due to the bubble by employing a point source and a dipole at the bubble centroid. He assumed that the bubble surface remains spherical. The formation, rise and eruption of a single bubble in a two-dimensional gas-fluidised bed has been simulated numerically by Gidaspow (1986) and Kuipers et al. (1992a, 1992b), using the TFM. Fluidised beds containing obstructions with different shapes and configurations have also been investigated numerically. For example, Lyczkowski et al. (1993) simulated the solid phase velocity profile and porosity distributions in a fluidised bed consisting of a immersed tube bank. Other numerical simulations of fluidised beds can be found in the works of Christie et al. (1998), Pain et al. (1998), Hu (1996), Kuipers et al. (1992a, 1992b), Ding and Gidaspow (1990) and Bouillard et al. (1989). Additional details of the history of fluidised bed modelling, together with various continuous modelling approaches, are given by Enwald et al. (1996). Hydrodynamic behaviour of fluidised beds has been investigated by Geldart (1986), Davidson et al. (1985) and Lim et al. (1995).

Many two-fluid models used in the literature suffer from uncertainties in prescribing the viscosity and normal stress of the solids phase (Ding and Gidaspow, 1990). Various non-Newtonian models for the internal stresses of the solid phase have been proposed, (see, for example, Gidaspow and Ettehadieh, 1983; Gidaspow, 1986). These viscosities were correlated with experimental observations. However, the need for a more systematic way of prescribing

viscosity has lead to the popularity of the granular temperature model (Chapman and Cowling, 1970; Savage, 1983; Shahinpoor and Ahmadi, 1983; Jenkins and Savage, 1983; Lun et al., 1984; Johnson and Jackson, 1987). The work of Ocone and Astarita (1993), which is based on an analogy between kinetic theory of gases and binary particle–particle collisions, provides a means of calculating the internal stresses for the solid phase without resorting to correlations. Investigations by Cao and Ahmadi (1995), Samuelsberg and Hjertager (1996) and Ding and Gidaspow (1990) have shown the ability of the two-fluid granular temperature approach to model, numerically, bubbling gas–solid fluidised beds.

This paper describes the results of the numerical modelling of gas–solid fluidised beds using the two-fluid granular temperature approach. The basis of the numerical model is a transient, mixed finite element discretization, which is used to solve the multi-phase equations with a discontinuous finite element representation of the granular temperature and continuity equations and a Petrov–Galerkin discretization of the momentum equations. The advantage of using this finite element scheme is that it has been proven stable and is capable of addressing geometrically-complex fluidised bed configurations.

Two different fluidised beds involving incompressible, isothermal mixtures with no phase exchange have been studied: the first is a slugging fluidised bed and the second a bubbling fluidised bed with an obstruction. Various phenomena that have been observed in fluidised beds but have not been subject to a numerical investigation, until now, are analysed. In both fluidised beds studied, the gas (air), at room temperature, enters from bottom of the bed and exits from the top, while the solid phase (spherical particles) circulates inside the bed.

The next section provides an overview of the CFD modelling, the governing equations solved and appropriate boundary conditions. Section 3 presents simulation results of a fluidised bed of D-particles (in Geldart's, (1986), Classification) operating mainly in a slugging regime. Comparison has been made between the existing experimental data and the results of the simulations. Various phenomena in the two-phase flow such as formation, coalescence, elongation and eruption of bubbles have been simulated and compared with the qualitative description of behaviour of bubbles available in the literature. The results of the simulations are compared for cylindrical and Cartesian coordinates, and the effect of breaking symmetry on the solutions, in Cartesian coordinates, has been investigated. In Section 4, fluidised beds containing both spherical and cylindrical obstructions in the central region of the bed have been simulated. Velocity profiles obtained from the simulation and experiment are compared.

2. Physical and numerical model description

In this section, the governing equations of gas–solid fluidised beds are presented along with the appropriate boundary conditions. The details of the numerical finite element discretization and solution of these equations are given in Pain et al. (1998). In summary, the numerical model is a transient, mixed finite element method that uses quadrilateral elements with a bi-linear variation of velocity and a discontinuous piece-wise-constant variation of volume fraction, pressure and granular temperature. The momentum equations are discretised using a Crank–Nicholson time-stepping method and a Petrov–Galerkin discretisation in space. This model has been incorporated into the general purpose CFD code FLUIDITY. One of the main

features of the code is that the finite element discretisation employed does not introduce large artificial dissipation into the fluids calculation which is extremely important when tracking bubbles through a fluidised bed.

2.1. Governing equations

The derivation of the governing equations of gas–solid dynamics can be found in Ding and Gidaspow (1990), and the boundary conditions in Hui et al. (1984). In the examples considered in this paper, both phases are assumed incompressible, which is a reasonable approximation of the adiabatic flows presented in the applications sections.

Although Enwald et al. (1999b) have shown some effects at high pressures (larger gas densities and therefore greater inertial forces) of gas phase turbulence, this has been ignored in this work because of the considerable addition uncertainties in the model closures. In addition, gas phase turbulent suppression is large for densely packed beds, motivating the neglect of these effects, e.g., Ding and Gidaspow (1990).

- Continuity equation for phase k:

$$\frac{\partial}{\partial t}(\alpha_k \rho_k) + \frac{\partial}{\partial x_i}(\alpha_k \rho_k v_{ki}) = 0. \tag{1}$$

  where $k = g$ denotes gas, $k = s$ denotes solid particles, ρ_k is the density of phase k, α_k the volume fraction of phase k, v_k the velocity of phase k, t is time and x_i is the ith spatial coordinate.
- Momentum equation for phase k:

$$\frac{\partial}{\partial t}(\alpha_k \rho_k v_{ki}) + \frac{\partial}{\partial x_j}(\alpha_k \rho_k v_{ki} v_{kj}) = -\alpha_k \frac{\partial p_g}{\partial x_i} + \alpha_k \rho_k g_i + \beta(v_{k'i} - v_{ki}) + \frac{\partial}{\partial x_i}(\tau_{kij}) - \Gamma_k v_{ki} \tag{2}$$

  where p_g is the pressure of the gas phase, g is gravity, β is the friction coefficient and Γ_s is the frictional force exerted on the solid phase by the wall (see next subsection) and Γ_g describes the friction between the gas and the wall — this is calculated from Blasius's equation (47) with a length scale equal to the height of the fluidised bed.
- Gas phase Newtonian viscous stress:

$$\tau_{g_{ij}} = 2\alpha_g \mu_g \left(\frac{1}{2}\left(\frac{\partial v_{g_i}}{\partial x_j} + \frac{\partial v_{g_j}}{\partial x_i} \right) - \frac{1}{3}\frac{\partial v_{g_k}}{\partial x_k} \right) \tag{3}$$

- Solids phase stress tensor:

$$\tau_{s_{ij}} = \left(-p_s + \alpha_s \zeta_s \frac{\partial v_{s_k}}{\partial x_k} \right)\delta_{ij} + +2\alpha_s \mu_s \left(\frac{1}{2}\left(\frac{\partial v_{s_i}}{\partial x_j} + \frac{\partial v_{s_j}}{\partial x_i} \right) - \frac{1}{3}\frac{\partial v_{s_k}}{\partial x_k} \right) \tag{4}$$

- Solids pressure:

$$p_s = \alpha_s \rho_s \left[1 + 2(1+e)\alpha_s g_0 \right] T \tag{5}$$

where e is the particle–particle restitution coefficient and T is the granular temperature.

- Solids shear viscosity:

$$\mu_s = \frac{4}{5}\alpha_s\rho_s d_s g_0(1+e)\left(\frac{T}{\pi}\right)^{\frac{1}{2}} \tag{6}$$

where d_s is the diameter of the fluidised particles.

- Solids bulk viscosity:

$$\zeta_s = \frac{4}{3}\alpha_s\rho_s d_s g_0(1+e)\left(\frac{T}{\pi}\right)^{\frac{1}{2}} \tag{7}$$

Various correlations are reported in the literature for the radial distribution function g_0, see Ding and Gidaspow (1990), Johnson and Jackson (1987), Ma and Ahmadi (1986), Carnahan and Starling (1969). We use a correlation proposed by Johnson and Jackson (1987) but amended to produce an improved fit to the results presented in Carnahan and Starling (1969):

$$g_0 = \frac{3}{5}\left[1-\left(\frac{\alpha_s}{\alpha_*}\right)^{\frac{1}{3}}\right]^{-1} \tag{8}$$

- Gas–solid friction coefficient (from Ergun equation) for $\alpha_g < 0.8$

$$\beta = 150\frac{(\alpha_s)^2\mu_g}{\alpha_g d_s^2} + 1.75\frac{\rho_g\alpha_s|v_g - v_s|}{d_s} \tag{9}$$

(μ_g is the dynamic viscosity of the gas phase) and for $\alpha_g > 0.8$

$$\beta = \frac{3}{4}C_d\frac{\alpha_g\alpha_s\rho_g|v_g - v_s|}{d_s}\alpha_g^{-2.65} \tag{10}$$

where, for $Re_s = \frac{\alpha_g\rho_g|v_g - v_s|d_s}{\mu_g} < 1000$

$$C_d = \frac{24}{Re_s}\left[1 + 0.15(Re_s)^{0.687}\right] \tag{11}$$

and for $Re_s > 1000$

$$C_d = 0.44 \tag{12}$$

- Fluctuation energy equation ($\frac{3}{2}T = \frac{1}{2}\bar{C}^2$) (where $\bar{C}$ is the mean particle velocity deviation form v_s)

$$\frac{3}{2}\left(\frac{\partial(\alpha_s\rho_s T)}{\partial t} + \frac{\partial}{\partial x_j}\left(\alpha_s\rho_s v_j T\right)\right) = \tau_{s_{ij}}\frac{\partial v_{s_i}}{\partial x_j} - \frac{\partial q_j}{\partial x_j} - \gamma - 3\beta T \tag{13}$$

- Collisional energy dissipation γ

$$\gamma = 3(1-e^2)(\alpha_s)^2\rho_s g_0 T\left[\frac{4}{d_s}\left(\frac{T}{\pi}\right)^{\frac{1}{2}} - \frac{\partial v_k}{\partial x_k}\right] \tag{14}$$

- Flux of fluctuating energy

$$q_j = -\kappa\frac{\partial T}{\partial x_j} \quad \text{where} \quad \kappa = 2\rho_s(\alpha_s)^2 g_0 d_s\left(\frac{T}{\pi}\right)^{\frac{1}{2}} \tag{15}$$

2.2. Boundary conditions

In order to solve the set of equations obtained for the gas–solid flow, appropriate boundary conditions for velocity and volume fraction of both phases and the granular temperatures of the solid phase are necessary. The volume fraction of gas is set to unity where gas enters the system (at the bottom inflow boundary). The particles may slip at the wall or bounce off the wall, creating complicated boundary conditions which will require simplification for use with the TFM.

The boundary conditions for gas and solid phases at the walls are: prescribed shear stress — obtained from Blasius equation for the gas (see Schlichting and Kestin, 1968) with a length scale equal to the height of the initial solid occupied domain (approximated with the shear stress of gas on a plane surface measured at a length equal to this height); no normal flow; prescribed fluctuating energy flux. At the top of the domain all components of the gas (air) stress tensor are set to zero allowing the gases to enter and leave the domain unhindered. Since pressure is the dominant part of the total normal stress component, this in effect sets the shared pressure level to zero at the topmost part of the domain (outlet boundary). Thus, the atmospheric pressure level must be added to this pressure where pressure is needed for compressible flow. No normal flow and zero shear stress conditions are applied to the solid phase at the topmost boundary (outlet), so there is no loss of solid in the simulations. In addition, at the inflow boundary the gas velocity component normal to the boundary is prescribed and zero gas shear stress conditions are used in the simulations.

Wall boundary conditions involving a wall–particle restitution coefficient, as described by Jenkins (1992) were used for the particulate phase. The boundary conditions applied to the particle phase can be summarised as follow: defining R as

$$R = \frac{7}{2}\left(\frac{1+e}{1+\beta_0}\right)\frac{S}{N}$$

where e is the wall restitution coefficient, β_0 the tangential coefficient of restitution, N the normal stress (the solid phase pressure is used here to approximate N) and S the shear stress. The shear stress at the wall can be calculated from the following correlation,

$$R = \begin{cases} \frac{3}{2}r, & 1 \le r \le \frac{2}{3}\mu_0 \\ \mu_0, & \frac{2}{3}\mu_0 \le r \le \infty \end{cases}.$$

where, $r = \frac{v_{\text{wall}}}{(3T)^{0.5}}$, $\mu_0 = \frac{7}{2}(\frac{1+e}{1+\beta_0})\mu$, in which, v_{wall} and T are the slip velocity and granular temperature of the particle near the wall and μ is the friction coefficient.

Let us define the normalised frictional flux, FF, by:

$$FF = \frac{7}{2}\left(\frac{1+e}{1+\beta_0}\right)\left[\frac{Q}{N\sqrt{3T}} + \frac{3}{8}(1-e)\right]$$

In Jenkins (1992), an expression for FF was determined

$$FF = \begin{cases} \frac{3}{8}\left[2(1+\beta_0)r^2 - (1-\beta_0)\right] & 1 \le r^2 \le \frac{1}{2}\left[\mu_0^2 + \frac{1-\beta_0}{1+\beta_0}\right] \\ \frac{3}{8}(1+\beta_0)\mu_0^2 & \frac{1}{2}\left[\mu_0^2 + \frac{1-\beta_0}{1+\beta_0}\right] \le r^2 \le \infty \end{cases}$$

where Q is the rate at which fluctuation energy is provided to the flow per unit area of the wall. This provides a convenient expression for $Q = q \cdot n$, which is applied in a natural finite element sense (Johnson, 1995).

3. Simulation of a slugging fluidised bed

The experimental apparatus operating in the Delft University of Technology (see van der Hagen et al., 1999), has been used to provide data to check the validity of the model. The bed consists of a 400 cm high cylindrical column with a diameter of 38.2 cm; the solid polystyrene particles have a density of 1.102 g/cm^3 and diameter 0.1899 cm. The gas phase is air at room temperature and enters the domain from the bottom of the bed, with a superficial velocity of 280 cm/s — 43% of the particle terminal velocity. The static bed height is 51 cm. A maximum packing factor of 57%, a particle–particle restitution coefficient of 0.99, a particle–wall restitution coefficient of 0.75 and a friction coefficient of 0.02 were used in the simulations, unless otherwise stated. These parameters were obtained from numerical experimentation in the absence of available data.

A uniform finite element grid of 20×60, in the x- and y-direction, respectively, was used in these simulations. Grid convergence was checked by repeating selected calculations with a 40×120 mesh. The frequency of the fine grid void fractions were very similar (see Section 3.1) to the coarser grid suggesting that grid convergence had been achieved. This may have been due to the bubbles being fairly large relative to the grid size for this problem. Time-step size convergence was also checked in a similar fashion: the step-size was reduced until frequency and void fractions for selected cases did not change significantly. An adequate converged time-step size value for the simulations was found to be 10^{-4} s. The 200 cm height domain used for the simulation was shown to be adequate in order to minimise the effect of the imposed outlet boundary conditions on the main flow.

3.1. Results and discussion

Based on the particle size and the density difference between particles and air, the solid phase can be classified as Geldart group D powder (Geldart, 1986). Using the second form of the Thonglimp (1981) correlation, the minimum fluidisation velocity was calculated to be 62 cm/s — 22% of the gas inlet velocity.

Initially, axi-symmetric cylindrical coordinates were used in the simulations. These initial results showed that, due to the highly three-dimensional nature of the problem, cylindrical coordinates produced results which were not consistent with experiments. For example, a high concentration of particles along the central axis was observed, see Fig. 9(a). The reason was that using axi-symmetric coordinates and hence applying a no-normal flow boundary condition along the central axis, prohibits particles from crossing the central axis. This acts in a similar manner to a vertical wall and so can result in a high local particle concentration. Since a three-dimensional simulation of the flow would be very demanding in resources, the simulation was performed using 2D Cartesian coordinates instead. To overcome the problem of having high concentration of particles in the centre of the reactor, the symmetry was broken by changing the direction of the gravity up to 1% for a short period of time - the first second of simulation. Results are time-averaged over 15 s of the simulations.

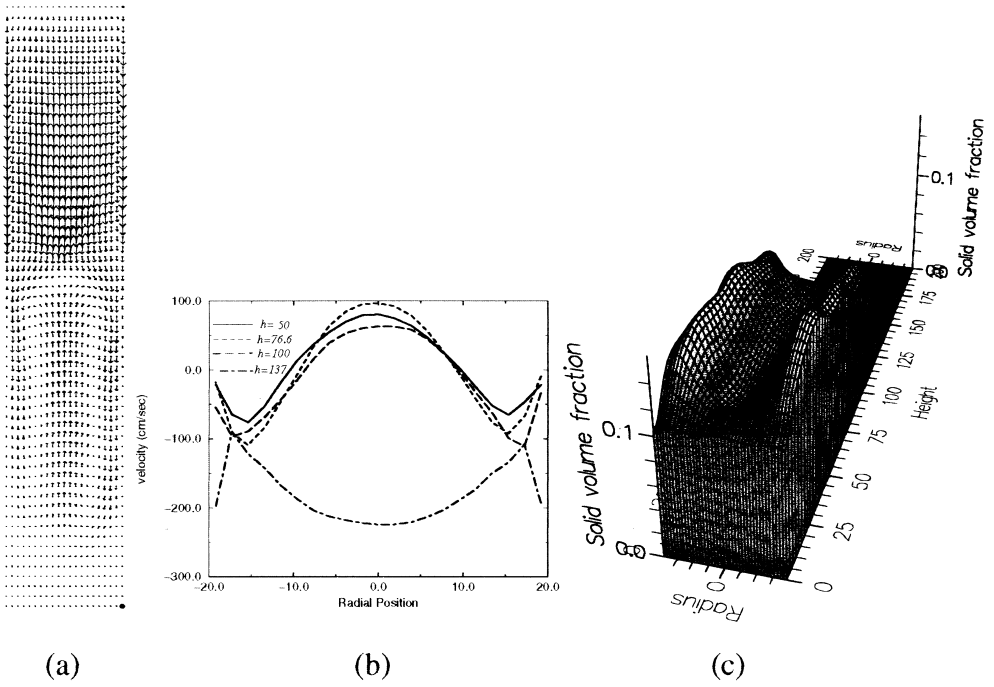

Fig. 1. Fluidised bed in the slugging regime: (a) time-averaged velocity vectors of particles. In the time-average sense the particles move upwards near the centre and fall down close to the walls. The maximum velocity in this graph is 233 cm/s. (b) Time-averaged stream-wise velocity distribution of particles at various heights in the bed. (c) Time-averaged volume fraction distribution of the particles inside the bed.

Fig. 1(a) shows the average velocity vectors of particles and indicates that particles move upwards at the centre of the bed and fall down near the wall. Fig. 1(b) illustrates the time-averaged velocity distribution of particles, in the vertical direction, at various heights of the bed. As can be seen, within a radius of 10 cm, particles are rising in the centre of the bed and falling down close to the wall. This phenomena is consistent with the description of the experiment by van der Hagen et al., which states that: "bubbles are moving upward in the centre of the zone and particles are falling along the bed wall". Fig. 1(c) shows the time-averaged volume fraction of solid particles inside the bed and indicates enhanced voidage in the central region and a high volume fraction of particles near the wall. This behaviour has been reported in many experiments. Gajdos and Bierl (1978) and Qin and Liu (1982) appear to have been the first to present radial voidage profiles showing high voidage in the centre and lower voidage close to the wall (Lim et al., 1995).

Power spectra of the fluctuation of the particle volume fraction were calculated at various positions along the central axis of the bed ($z = 57$, 77, 99 cm) and 1 cm from the walls. The results indicate that different positions of the bed oscillate with different frequencies, ranging from 0.7 to 1.4 Hz. This is consistent with the results of van der Hagen et al. experiments who report: "the auto power spectral density of gamma signal was calculated in order to study the frequency distribution of gas fraction fluctuations. A dominant frequency band of 1–1.5 Hz appeared in the spectra, both for central and peripheral measurements at all axial positions". These frequencies compare well with those of the Baskakov et al. (1986) equation for frequency $(\frac{1}{\pi}(\frac{g}{H_{\mathrm{mf}}})^{\frac{1}{2}} \approx 1.2)$, which is a theoretical model based on the release of a single bubble at a time from the bed, and an analogy with the oscillations under gravity of liquid in a U-tube. H_{mf} is the bed height at minimum fluidisation velocity U_{mf}. Baskakov's equation results also agree with the equation of Roy et al. (1990), which states that the frequency f is related to the speed of sound c according to $f = c/4H$ for a fluidised bed of height H in which $c = (\mathrm{d}p/\mathrm{d}\rho)^{\frac{1}{2}}$ with ρ being the bulk density of the bed.

The time-averaged granular temperature, defined as $\frac{3}{2}T = \frac{1}{2}(\bar{C})^2$, where $\bar{C}$ is the fluctuation velocity of the particulate phase, is shown in Fig. 2. It is relatively large near the top of the bed and is also larger near the wall than in the central region of the bed. The reason is that, near the top of the bed, some particles are falling while others are still rising. This creates a large particle shear stress in this region. Shear stresses close to the walls are also large, due to the concentration of particles and the relatively large velocity gradient of the particulate phase.

3.1.1. Coalescence of bubbles

As a result of bubble coalescence, large bubbles form in the middle of the bed. Various mechanisms are reported in the literature for the coalescence of bubbles. Clift and Grace (1985) explain that, assuming two bubbles centred on a common vertical line rise vertically, the lower bubble accelerates under the influence of the leader so that coalescence occurs when the lower bubble catches up. For bubbles not in vertical alignment, Toei et al. (1967) explain that the lower bubble moves towards the line of rise of the upper, subsequently accelerating vertically to enter its wake, so that coalescence occurs typically with the bubble alignment almost vertical. However, Cranfield and Geldart (1974) explain that "Coalescence in group D beds is much less understood: qualitatively, bubbles appear to grow by absorbing gas from neighbouring bubbles rather than as a result of relative bubble motion".

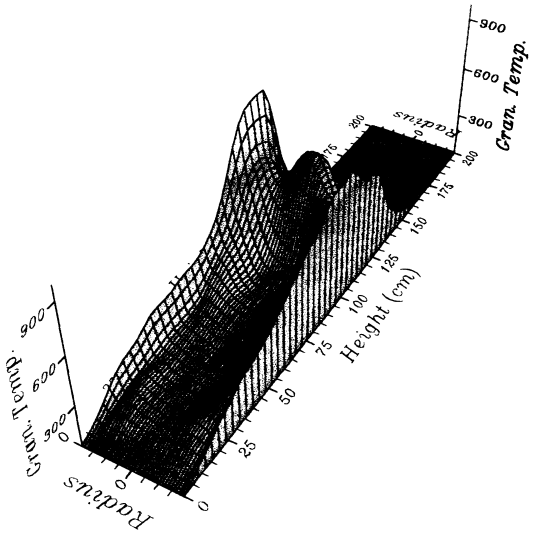

Fig. 2. Time averaged granular temperature of particles for fluidised bed in the slugging regime (simulation performed in Cartesian coordinates) maximum temperature in diagram is 920 cm^2/s^2.

Fig. 3 shows the modelled process of coalescence of bubbles. As can be seen, bubbles that are created near the bottom corners of the bed at $t = 7.4$ s, have moved towards the centre and the line of rise of the upper bubble, by time $t = 7.5$ s. At $t = 7.6$ s, the bubble in the centre has entered into the wake of the upper bubble, and at $t = 7.7$ s the bubbles have coalesced. This

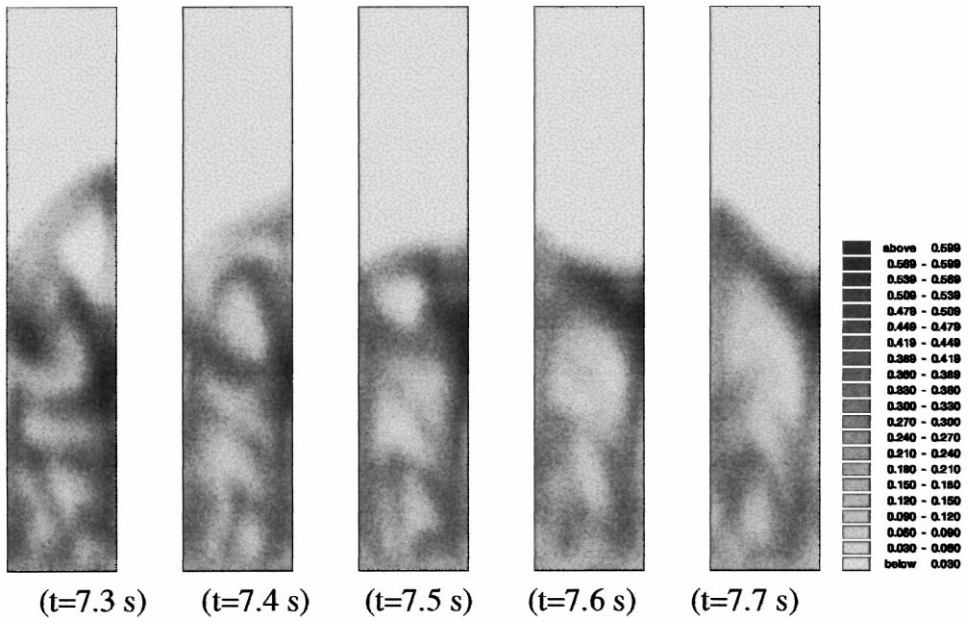

Fig. 3. Distribution of volume fraction of particles in the slugging fluidised bed.

coalescence behaviour is consistent with the explanation of Clift and Grace (1985). As a result of coalescence near the top of the bed, bubbles near the top are larger than these near the bottom of the bed. Since, at the top of the bed, the size of the bubble is comparable with the diameter of the bed, this fluidised bed mainly works in the slugging regime. Fig. 4 illustrates the corresponding velocity vectors of the spherical particles. Velocity vectors of the gas phase are shown in Fig. 5. Gas flows into the base of the bubble and out of the top, a behaviour that is characteristic of group D Geldart powders. In this group, for large particle systems, all but the largest bubbles travel slower than the interstitial gas, and gas short-circuits the bed by entering the bottom of a bubble and leaving the top (Geldart, 1986). This is seen on comparing the positions of the bubbles/slugs in Fig. 3 and the corresponding gas velocities in Fig. 5.

3.1.2. Elongation of bubbles

Bubbles are subject to elongation when rising along vertical tubes (Grace and Harrison, 1967), or during interaction with walls or other bubbles. This simulation showed that the walls have an important role in the elongation of bubbles. Fig. 6 shows the elongation of a bubble along the central axis of the bed, obtained in these simulations. The effect of the walls in changing the direction of motion of the bubble is clearly illustrated by the 'S' shaped slugs. The corresponding velocity vectors of particles and gas are shown in Fig. 7. Two counter-

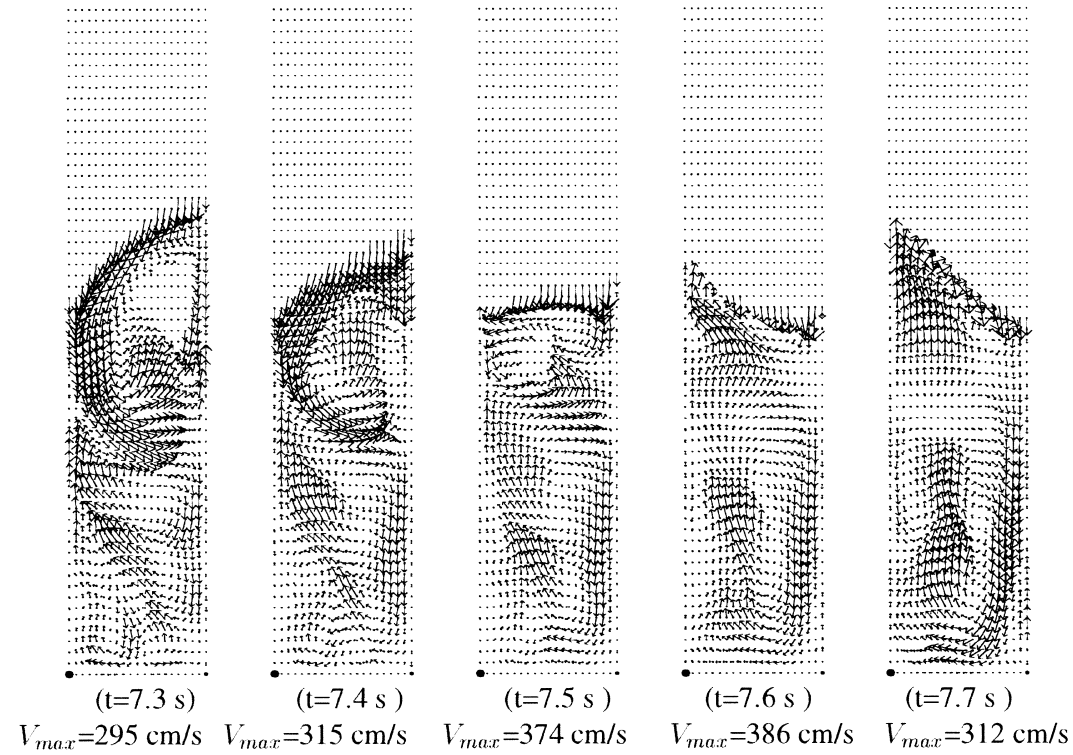

Fig. 4. Velocity vectors, at various times of the particle phase for the slugging fluidised bed, indicating how bubbles coalesce.

rotating vortices behind the large bubble, at time $t = 6.2$ s, can be seen in the particle velocity vectors. Also, it can be seen that two secondary bubbles appear at the centre of these vortices, apparently created by centrifugal forces. The flow of particles in this case is quite similar to the flow of a fluid past a bluff body. This behaviour was reported for the first time by Davies and Taylor (1950). Again, it can be seen, from the velocity vectors of the gas phase, that gas enters from the base of the bubble and out of the top.

3.1.3. Eruption at the bed surface

Clift and Grace (1985) explain that, as a bubble approaches the upper free surface of a fluidised bed, a dome is seen to rise in advance of the bubble. A mantle of solids separating the top of the dome from the roof of the bubble thins, until the bubble breaks through. Similar behaviour can be observed in the volume fraction distribution of the particles shown in Fig. 8. Periodically, relatively large bubbles burst through the bed surface, the bed collapses rapidly and new bubbles slowly re-expand the bed.

3.1.4. Comparison between the results of simulations in cylindrical and Cartesian coordinates

The simulations showed that, the use of axi-symmetric cylindrical coordinates, can result in an unphysical high concentration of spherical particles in the central region of the reactor. As mentioned earlier, this is due to the no-normal flow boundary condition at the central axis of

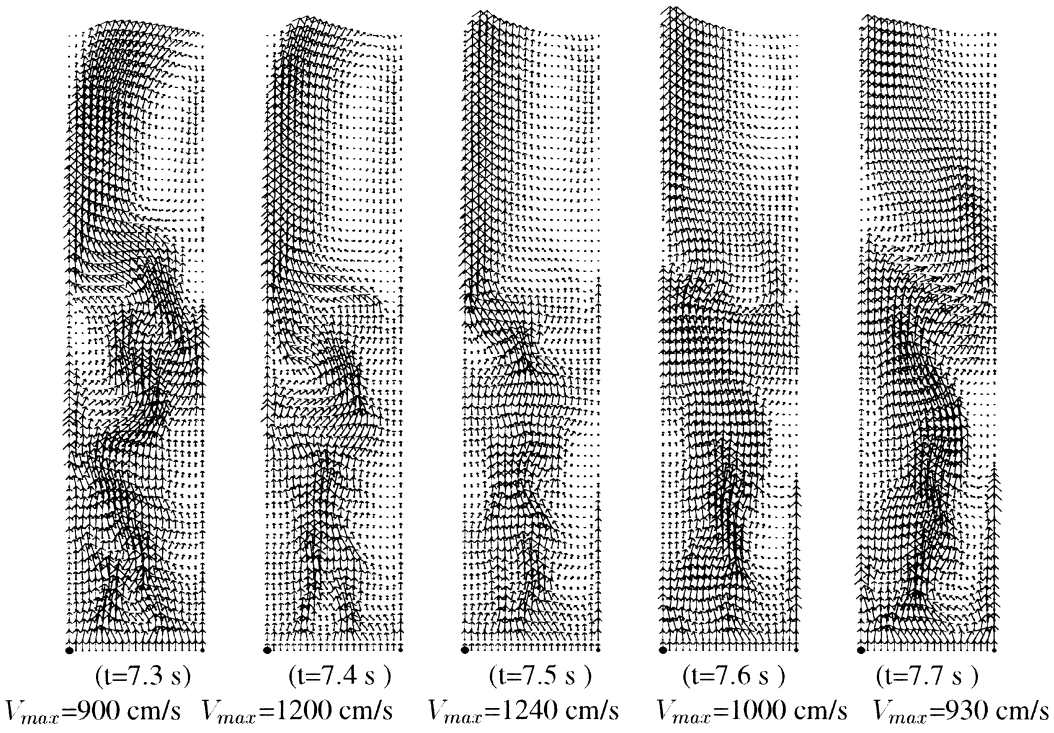

Fig. 5. Velocity vectors, at various times, of the gas phase for the slugging fluidised bed, indicating how bubbles coalesce.

the cylinder, applied in this system of coordinates. Various experiments have shown that the central region should have a low concentration of particles. Applying a symmetrical boundary and initial conditions in two-dimensional Cartesian coordinates results in the same problem. However, when the symmetry is broken, the results of simulation are in closer agreement with the experiment.

Some of these difficulties with axi-symmetric cylindrical coordinates have been circumvent in Sun and Gidaspow (1999) by integrating the TFM equations between $r = +$ve and $r = -$ve extremes of the modelling domain and placing a donner cell on the $r = 0$ line so that information can travel between $r = +$ve and $r = -$ve of the domain. However, we believe this is purely a numerical artifact and that in the continuum in axi-symmetric coordinates no information can travel through this line. The axi-symmetric assumption does not allways lead to these physically unrealistic flows, for example, Gidaspow (1994) shows that both cases are possible depending on the flow rate, bed height and geometry.

Fig. 9(a) and (b) compare the time averaged distribution of particles obtained from the calculations in the cylindrical and Cartesian coordinates (in the latter case when symmetry is broken). As can be seen in this figures, the two geometries give rise to different particle distributions. A dynamic study showed that, in Cartesian coordinates, the correlation dimension of this bed is about 1.8, and the system has a positive Lyapunov exponent, indicating that this fluidised bed is chaotic according to Wolf et al. (1985). Since there always exists asymmetry in particle interactions and geometry in a fluidised bed, and, since in chaotic systems a very small perturbation grows exponentially, the whole system becomes asymmetric after a short period of time. However, as shown in Fig. 9, the time-averaged results are

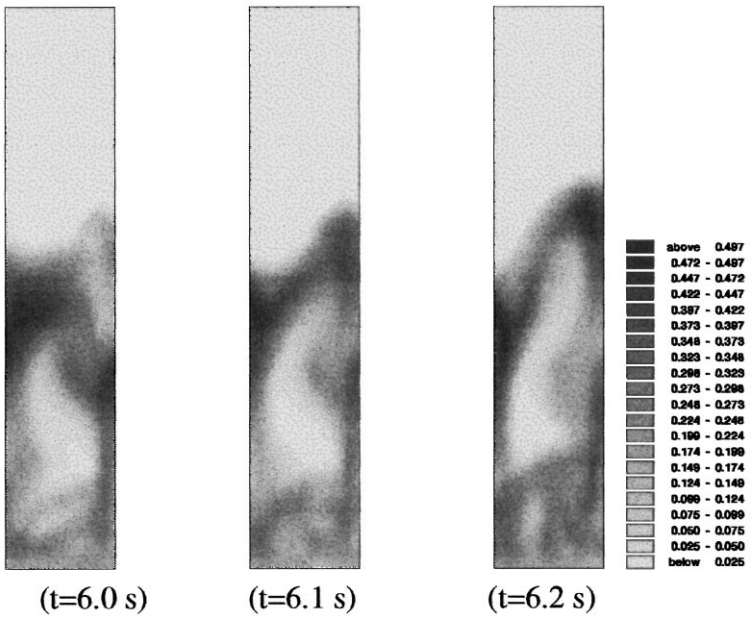

Fig. 6. Distribution of volume fraction of particles in slugging fluidised bed, indicating the elongation of a bubble.

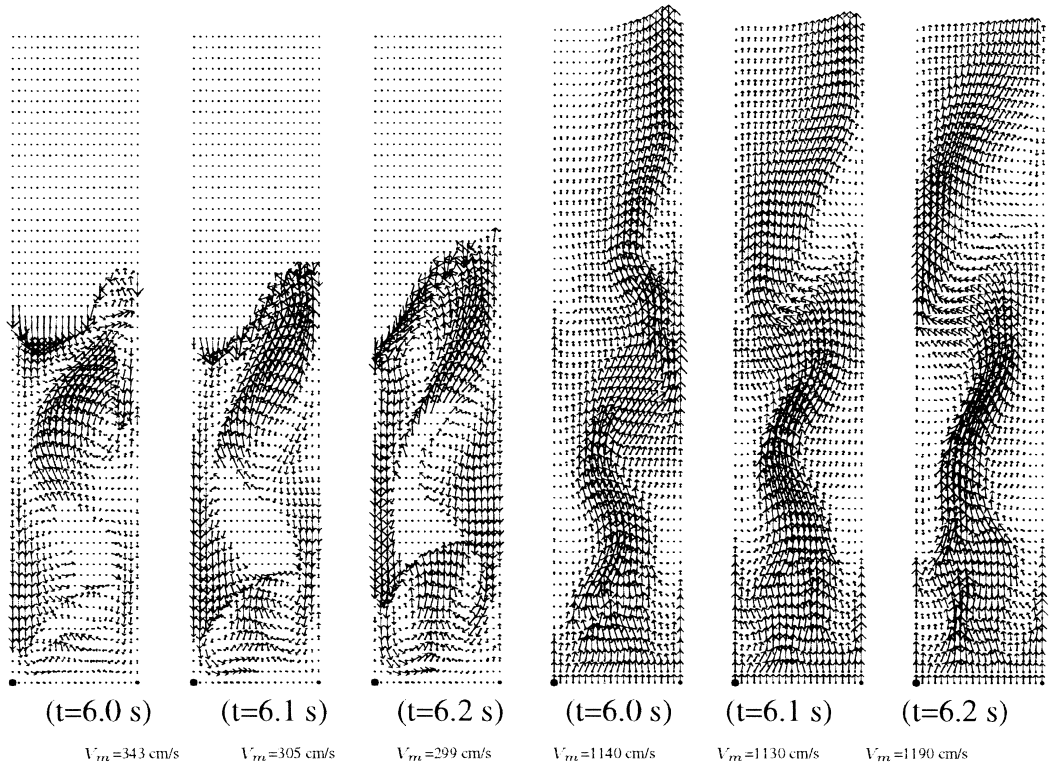

Fig. 7. Slugging fluidised bed: the first three figures show the velocity vectors of particles and the next three indicate the velocity vectors of the gas phase, when a bubble elongates.

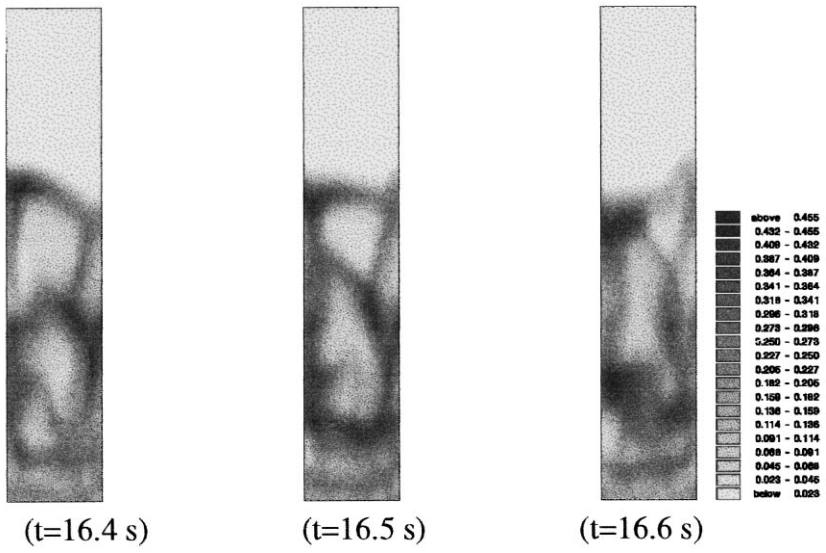

Fig. 8. Eruption of a bubble at the surface of the slugging fluidised bed.

symmetric (particles fall down near the wall and rise in the central region), suggesting that 15 s is a sufficient time window to study the dynamics of this system.

3.1.5. The effect of material-particle parameters on the simulations

The appropriate values of some modelling parameters, such as the restitution coefficient of spherical particles, the friction coefficient at the wall and the wall restitution coefficient are not available. To explore the effect of each of these parameters on the results, simulations should be repeated when one of these parameters is changed while the others are fixed. Obviously, this process is expensive and time consuming. Our simulation results (not shown here) demonstrated that simulations are sensitive to the wall friction coefficient and are less sensitive to the particle–particle and particle–wall restitution coefficients. Restitution coefficients indicate the amount of energy dissipation due to the collision of particles. To show the influence of these parameters, the results of simulations with a wall friction factor of 0.2 are compared with the results of simulations with a wall friction factor of 0.02. Fig. 9(b) and (c) show the time-averaged distribution of the volume fraction of particles for the two cases. Fig. 10(a) and (b) illustrates the variation of void fraction at various heights for these two cases. When a lower wall friction factor is used in the calculations, the radial distribution of void fraction is more uniform. Fig. 10(a) and (b) also show that, when a lower wall friction coefficient is used, the concentration of particles at lower regions of the bed, e.g., $h = 77$ cm, is larger. This occurs because, as mentioned earlier, particles, in the time-average sense, are descending near the walls and, when a relatively smaller wall friction coefficient is used, they can slide more easily and

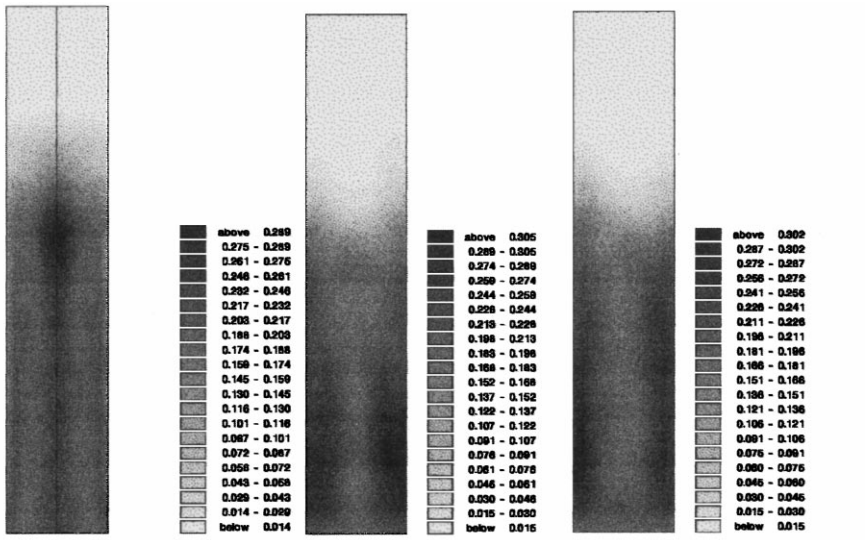

Fig. 9. Comparison between the time-averaged distribution of volume fraction of particles for a slugging fluidised bed: (a) axi-symmetric cylindrical and (b) Cartesian coordinates; (c) time-averaged distribution of volume fraction of particles when a relatively low wall friction coefficient $\mu = 0.02$ is used, in Cartesian coordinates.

accumulate at the lower regions (see also Fig. 9(b) and (c)). The corresponding experimental results are shown in Fig. 10(c). Comparison between experimental results and the simulations shows that, while the radial distribution of the void fractions in the simulations are qualitatively close to that of the experiments, the axial distributions are different. The void fractions in the experiments are higher than that at the corresponding height in the simulations.

4. Solid flow in the presence of a spherical/cylindrical obstruction

A further numerical investigation was carried out for a fluidised bed with an obstacle placed near the centre, representing equipment which might normally be used inside fluidised beds, e.g., a heater. The schematic of the reactor is shown in Fig. 11(a). The study was conducted using both axi-simmetric r–z and x–y Cartesian 2D geometries. In the former, the obstruction took the shape of a sphere and in the latter a cylinder.

Air with uniform inlet velocity, $U_0 = 47.6$ cm/s — 13% of the terminal velocity of the particles — enters from the bottom of the bed, at room temperature. The static bed height of the reactor is 15 cm, when filled with spherical glass beads of diameter in the range of 0.042–0.06 cm. The diameter of the fluidised bed is 13.8 cm and the height is 25 cm. A corresponding experiment has been conducted by Lin et al. (1985). A restitution coefficient of 0.98 was assumed for both particle–particle and particle–wall collisions, together with a wall friction coefficient of 0.02. The diameter of the glass beads was assumed to be 0.5 mm.

Fig. 11(b) shows the grid structure used in the axi-symmetric cylindrical coordinates simulation which contained a total of 600 elements (671 nodes). The 2D x–y Cartesian coordinates simulation used a mesh with 2400 elements (2520 nodes). The region of large void fraction appearing below the obstruction, which is periodically shed, has a frequency which was proven to be grid-resolved in both simulations. A time-step size converged value of 10^{-4} s was used in the simulations.

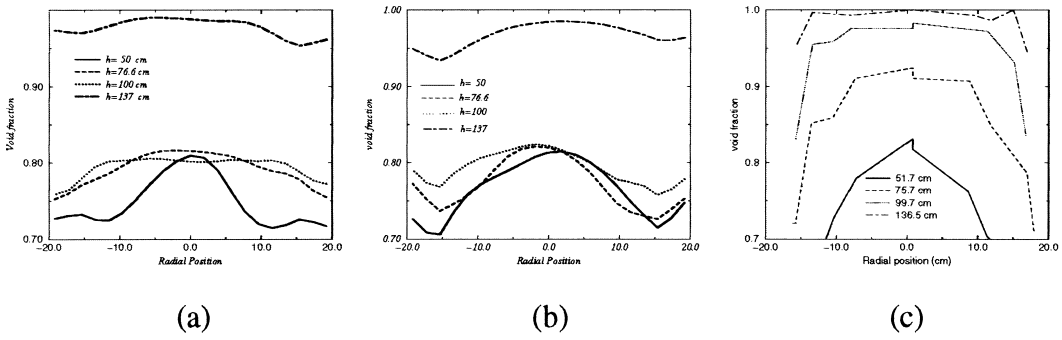

Fig. 10. Comparison between the time-averaged void fraction distribution for slugging fluidised bed, at various heights, when wall friction coefficients of (a) 0.02 and (b) 0.2 are used; (c) experimental results.

4.1. Results and discussion

Based on particle size and the density difference between particles and air, the solid phase can be classified as Group B of Geldart powders. The minimum fluidisation velocity for this reactor is about 19.5 cm/s and, since the Froude number, u_{mf}^2/gd is greater than unity, it may be expected that the reactor will operate in an aggregative state in which bubbles play a major role in the dynamical behaviour.

Fig. 12(b) shows the modelled time-averaged velocity vectors of the glass beads. This figure demonstrates that, in the time-average sense, there is a circulation of particles in which they Ascend near the Centre and Descend near the Wall (ACDW). However, a weak Ascending near the Wall and Descending near the Centre (AWDC) in the region below the sphere has been reported in the experiment (Lin et al., 1985). The corresponding experimental result is shown in Fig. 12(c). As can be seen from this figure, there is a toroidal vortex with strong upward motion in the neighbourhood of the sphere and a downward flow near the wall. The same phenomenon can be observed in the velocity vectors of the particles from the simulations.

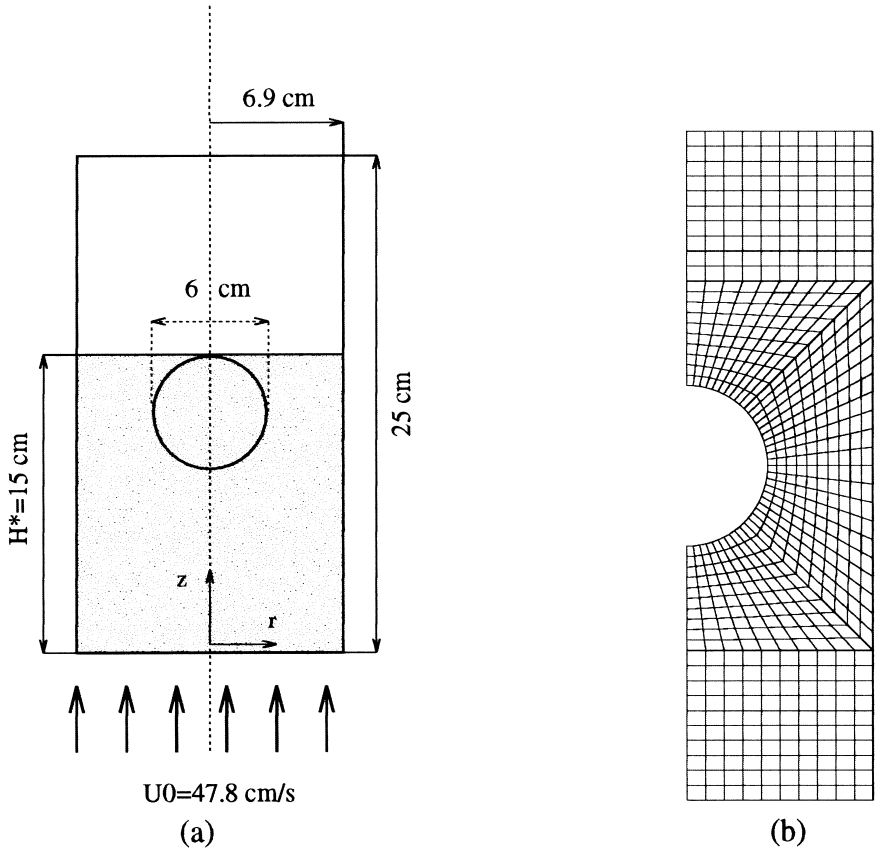

Fig. 11. (a) Schematic of the fluidised bed containing a spherical obstacle, H^* indicates the static bed height; (b) Grid structure in axi-symmetric cylindrical coordinates used for the simulation.

Comparing the results of the experiment with that of the simulation also indicates that there is a downward flow close to the surface of the supporting rod (see Fig. 12(c)). The same pattern of flow can be observed in the velocity vectors of the simulation. The velocity vectors of the gas phase is shown in Fig. 12(a).

Power spectra of fluctuations of the volume fraction of the glass beads for various positions are illustrated in Fig. 13 and indicate that the frequency of the oscillations varies between 4 and 5.2 Hz. A frequency range between 3.8 and 5 Hz for the ACDW region has been reported from the experiment performed by Lin et al. (1985).

The time-averaged volume fraction of glass beads is shown in Fig. 14(a). A high volume fraction of particles can be observed on the top of the sphere. This occurs because, as can be observed from the velocity vectors of the gas phase in Fig. 12, the gas flow separates from the surface of the sphere and thus, the drag force exerted by the gas on the particles is not appreciable and particles tend to accumulate there. A low volume fraction of particles can be observed near the lower part of the sphere. This is because the drag force in this region is not sufficiently large to fluidise the particles, and thus, they either fall or change their direction. A further phenomena observed in this simulation, and shown in Fig. 15, is that, in this region, (the lower part of the sphere), bubbles form periodically (also reported in Davidson et al., 1985, p. 474) and then move upwards next to the surface of the sphere. At the mid-plane

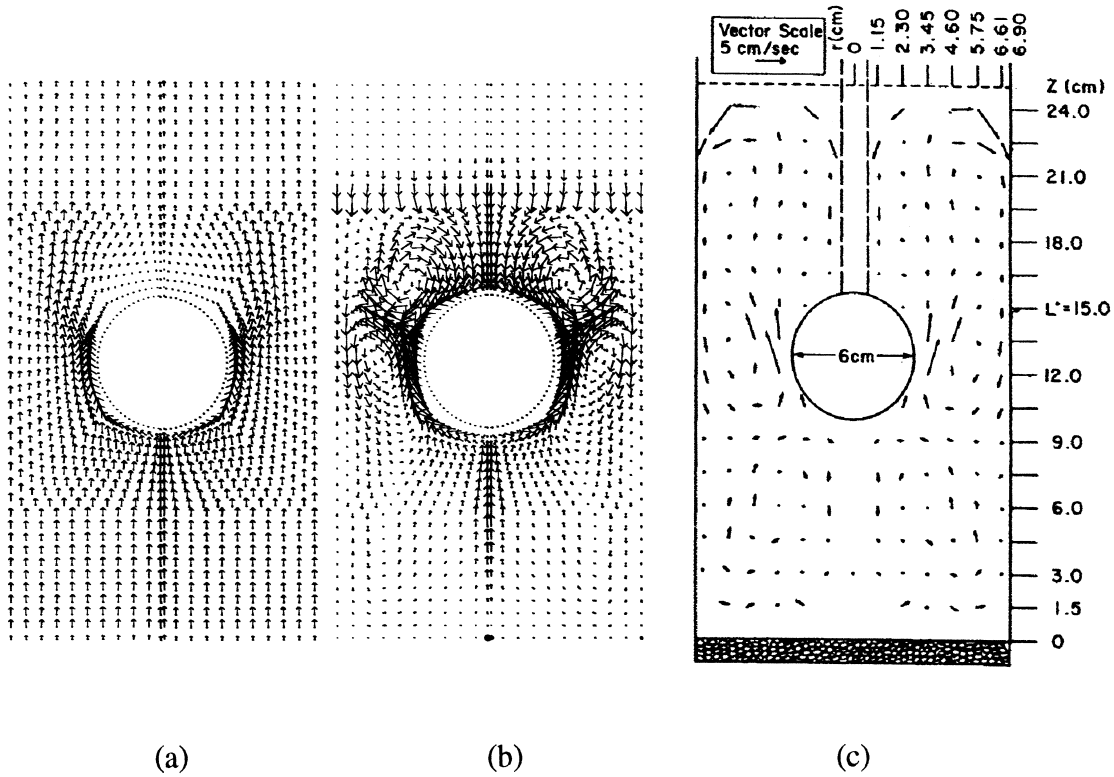

Fig. 12. Fluidised bed with obstruction: time-averaged velocity vectors of (a) the gas phase obtained from the simulations; (b) the particulate phase from the simulations; and (c) the particulate phase from the experiment.

height of the sphere, they separate from it and move up towards the bed surface. The granular temperature distribution, shown in Fig. 14(b) indicates a high granular temperature near the top of the bed and below the lower part of the sphere, the positions which have large fluctuations of velocity.

The poor quality of the solution in axi-symmetric coordinates for the previous simulation in the slugging regime motivated us, in the absence of a sufficiently efficient 3D model, to perform the simulation in 2D Cartesian coordinates and to break the central axis symmetry. The time required for 3D simulations can be prohibitive, however, parallel computing offers a possible solution. In Enwald et al. (1999a), a parallelised TFM was described along with a validation of their TFM against bubbling fluidised bed experiments. The fact that the simulations are not performed in 3D is not the only source of uncertainty with our model and similar models like the above. There exists considerable uncertainty in the validity of the TFM and the closure models used, thus, extensive validation of a model in each parameter regime seems to be required in order to have confidence in the TFM approach and even the authors' implementation of the TFM.

Fig. 16(a) shows the time-averaged volume fraction of the particulate phase for the Cartesian coordinate simulation, when the symmetry is broken. This figure indicates that, qualitatively, the pattern of volume fraction distribution is similar to that of the cylindrical coordinates. This

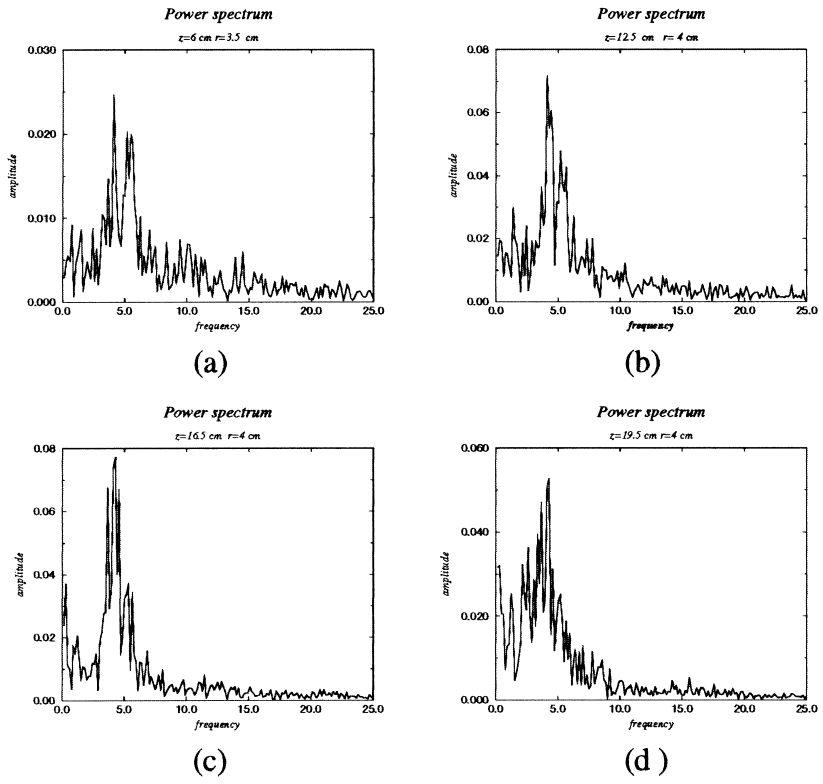

Fig. 13. Power spectrum at various positions in the fluidised bed with a spherical obstruction.

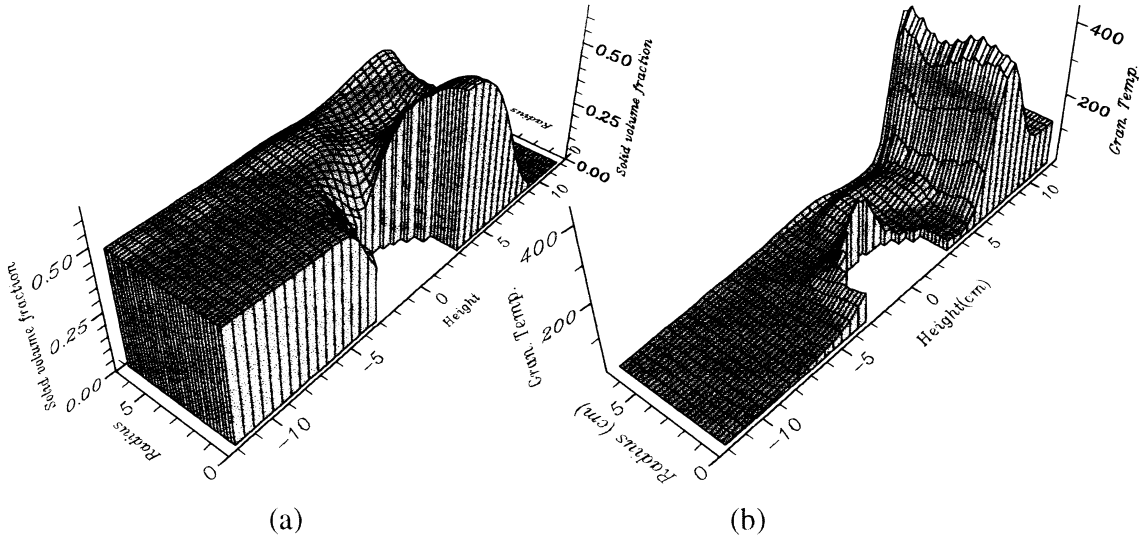

Fig. 14. Obstructed fluidised bed: (a) time-averaged volume fraction of particles. The maximum volume fraction of particles is 0.62 which is observed on top of the spherical particle; (b) time-averaged granular temperature of particles. The maximum granular temperature is about 440 cm^2/s^2.

suggests that the presence of the spherical obstacle (or cylindrical obstacle, in 2D Cartesian coordinates) minimises the effect of the no-normal flow condition applied in the central axis in cylindrical coordinates simulations. The granular temperature distribution shown in Fig. 16(b) and the particle and gas velocity vectors shown in Fig. 17(a) and (b) are almost similar to the

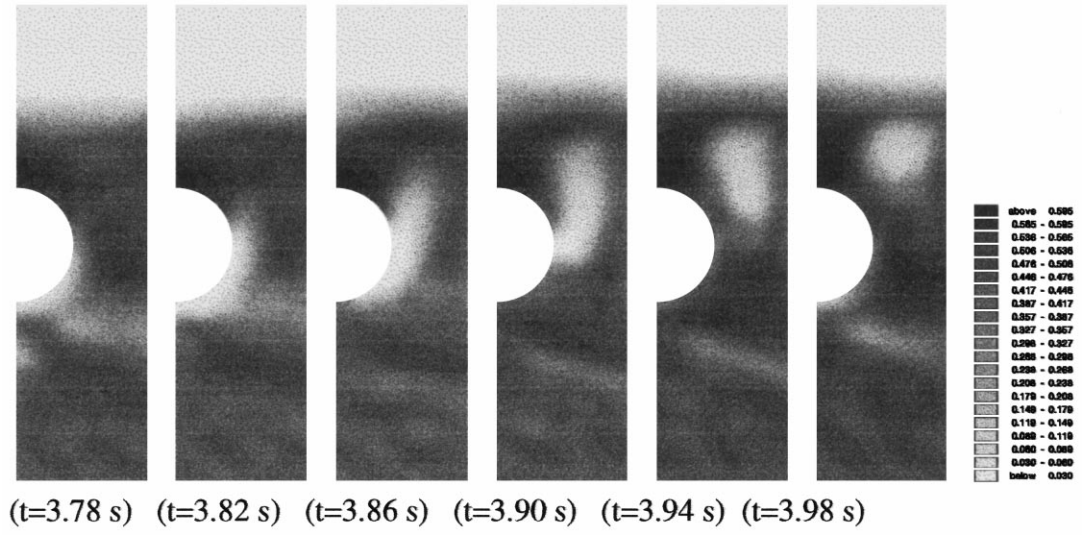

Fig. 15. A bubble, formed near the lower region of the spherical obstacle, separates and moves towards the surface of the bed.

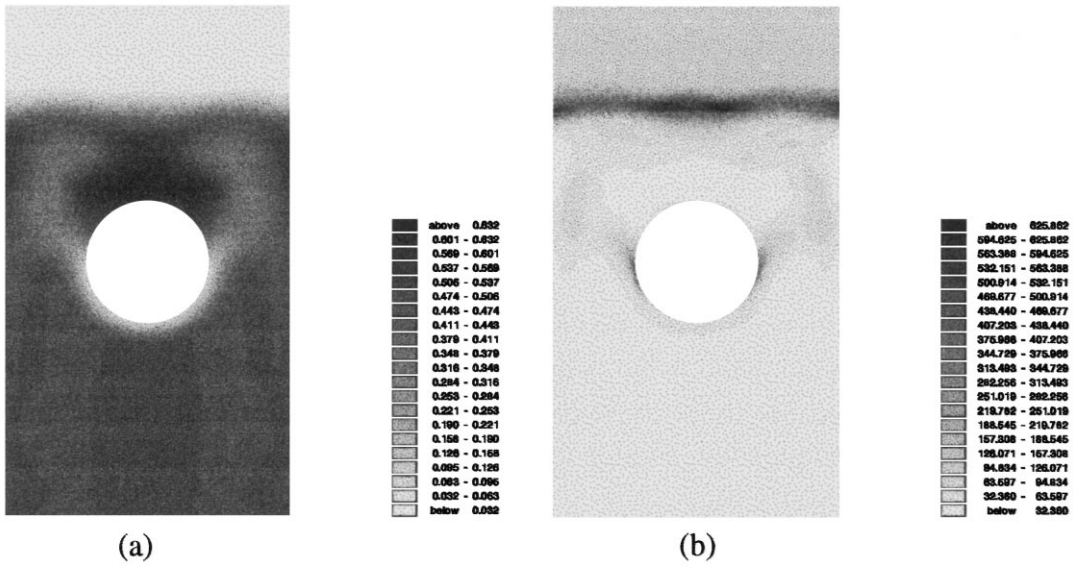

Fig. 16. Distribution of (a) volume fraction and (b) granular temperature of particles in 2D Cartesian coordinates for fluidised bed with obstruction.

results of simulations obtained from the cylindrical coordinates. Power spectra of the various positions in the bed are shown in Fig. 18. Again, a dominant frequency of 5 Hz can be observed in these figures.

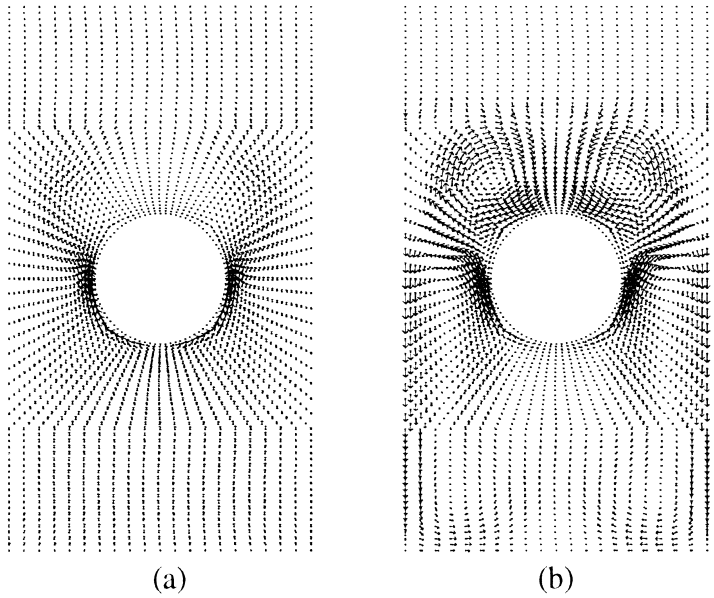

Fig. 17. Time-averaged velocity vectors of obstructed fluidised bed: (a) gas phase and (b) particulate phase, in 2D Cartesian coordinates, when the symmetry is broken.

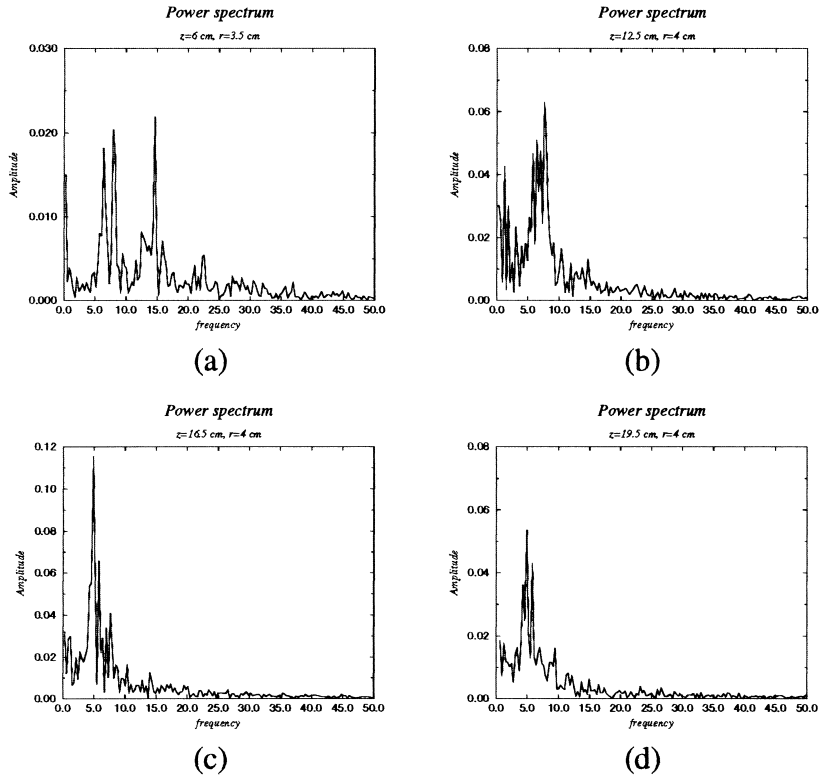

Fig. 18. Power spectrum for obstructed fluidised bed at various positions, obtained from simulations in Cartesian coordinates.

5. Conclusions

Numerical modelling, based on the two-fluid granular temperature model, has been used to simulate two different fluidised bed problems. In both cases, gas, (air at room temperature) enters from the bottom of the fluidised bed and exits from the top, while particles circulate inside the bed. The first simulation concerned a fluidised bed in the slugging regime with powders in group D of the Geldart classifications. Simulations in axi-symmetric cylindrical coordinates were performed and it was shown that imposing axi-symmetry can lead to unphysical results, e.g. a region with a high concentration of particles appears around the central axis. Therefore, a two dimensional Cartesian coordinate system was used and the symmetry was broken. The time-averaged distribution of particles showed that bubbles move in the central region of the bed and particles fall down along the bed wall. This type of behaviour is consistent with the results of experiments. The power spectrum of fluctuations of the particles showed that different parts of the bed oscillate with different frequencies, ranging from 0.7 to 1.4 Hz. This is also consistent with the results of the experiments which indicates a dominant frequency band of 1–1.5 Hz.

The simulations showed that the results are sensitive to material-particles parameters to various degrees. They are sensitive to wall friction coefficients but less sensitive to restitution

coefficients. A number of phenomenon such as formation, coalescence, elongation and eruption of bubbles were discussed and it was shown that, at least in some cases, bubbles are created by the centrifugal force of the particles.

The second case studied was related to the simulation of a fluidised bed which has in the central region of the bed an obstruction, representing equipment used inside industrial fluidised beds. Comparison between velocity vectors obtained from the simulations and from published experiment showed that, while at the top of the obstruction the results were consistent, in the region below a weak circulation — ascending flow near the wall and descending near the centre — appeared in the experiment which was not observed in the numerical simulations.

Since the particle/gas drag force behind the obstruction is insufficient to fluidise the particles, a high concentration of particles appears on the top of the sphere, indicating a poor fluidisation quality. The simulations also showed that near the lower part of the obstruction a void appears. This region of the obstruction probably experiences less erosion than the others. The calculated granular temperature distribution near the surface of the obstruction can be used to detect areas which are particularly susceptible to erosion.

Acknowledgements

We would like to acknowledge the research team in the Interfaculty Reactor Institute (IRI), Delft University of Technology for sharing their experimental results with the authors and for providing the initial motivation for this work. We would also like to thank Mr Adrian Umpleby for his computational support during the preparation of this paper.

References

Baskakov, A.P., Tuponogov, V.G., Filippovsky, N.F., 1986. A study of pressure fluctuations in a bubbling fluidised bed. Powder Tech. 45, 113–117.

Bouillard, J.X., Lyczkowski, R.W., Gidaspow, D., 1989. Porosity distributions in a fluidised bed with an immersed obstacle. AIChE Journal 35, 908–922.

Carnahan, N.F., Starling, K.E., 1969. Equation of state for nonattracting rigid spheres. The Journal of Chemical Physics 51, 635–636.

Cao, J., Ahmadi, G., 1995. Gas-particle two-phase turbulent flow in a vertical duct. Int. J. Multiphase Flow 21, 1203–1228.

Chapman, S., Cowling, T.G., 1970. The Mathematical Theory of Non-Uniform Gases. Cambridge University Press, Cambridge.

Christie, I., Ganser, G.H., Wilder, J.W., 1998. Numerical solution of a two-dimensional fluidised bed model. Int. J. Numer. Meth. Fluids 28, 381–394.

Clift, R., Grace, J.R. (Eds.), 1985. Continuous Bubbling and Slugging. Academic Press, London.

Cranfield, R.R., Geldart, D., 1974. Large particle fluidization. Chem. Eng. Sci. 29, 935–947.

Crowe, C., Sommerfield, M., Tsuji, Y., 1998. Multiphase Flows with Droplets and Particles. CRC Press, Boca Raton.

Davidson, J.F., Clift, R., Harrison, D. (Eds.), 1985. Fluidization, 2nd ed. Academic Press, London.

Davies, R.M., Taylor, G.I., 1950. Fluidization. Proc. R. Soc. London A 200, 375–390.

Ding, J., Gidaspow, D., 1990. A bubbling fluidization model using kinetic theory of granular flow. AIChE Journal 36, 523–538.

Enwald, H., Peirano, E., Almstedt, A.E., 1996. Eulerian two-phase flow theory applied to fluidization. Int. J. Multiphase Flow 22, 21–66.

Enwald, H., Peirano, E., Almstedt, A.E., Leckner, B., 1999a. Simulation of the fluid dynamics of a bubbling fluidised bed. Experimental validation of the two-fluid model and evaluation of a parallel mulit-block solver. Chem. Eng. Science 54, 311–328.

Enwald, H., Peirano, E., Almstedt, A.E., Leckner, B., 1999b. Fluid dynamics of a pressurized bed: comparision between numerical solutions from two-fluid models and experimental results. Chem. Eng. Science 54, 329–342.

Gajdos, L.J., Bierl, T.W., 1978. Studies in support of recirculating fluidized bed reactors for the processing of coal. Topical report on work performed under DOE/EX-C-76-01-2449. Carnegie-Mellon University, Pittsburgh, PA.

Geldart, D. (Ed.), 1986. Gas Fluidization Technology. Wiley, Chichester, UK.

Gera, D., Gautam, M., Tsuji, Y., Gawaguchi, T., Tanaka, T., 1998. Computer simulation of bubbles in large-particle fluidized beds. Powder Technology 98, 38–47.

Gidaspow, D., 1986. Hydrodynamics of fluidization and heat transfer: super computer modeling. App. Mech. Rev. 39, 1–23.

Gidaspow, D., 1994. Multiphase flow and fluidization continuum kinetic theory descriptions. Academic Press, New York.

Gidaspow, D., Ettehadieh, B., 1983. Fluidization in two dimensional beds with a jet. Part II: Hydrodynamic modelling. Iand EC Fundam. 22, 193–201.

Grace, J.R., Harrison, D., 1967. The influence of bubble shape on the rising velocities of large bubbles. Chem. Eng. Sci. 22, 1337–1347.

Harris, P.J., 1996. A numerical method for modelling the motion of a spherical bubble. Int. J. Numer. Meth. Fluids 22, 1125–1134.

Hu, H.H., 1996. Direct simulation of flows of solid–liquid mixtures. Int. J. Multiphase Flow 22, 335–352.

Hui, K., Haff, P.K., Ungar, J.E., 1984. Boundary conditions for high-shear grain flows. J. Fluid Mech. 145, 223–233.

Jenkins, J.T., 1992. Boundary conditions for rapid granular flow: flat, frictional walls. Transaction of the ASME 59, 120–127.

Jenkins, J.T., Savage, S.B., 1983. A theory for the rapid flow of identical, smooth, nearly elastic spherical particles. J. Fluid Mech. 130, 187–202.

Johnson, C., 1995. Numerical Solution of Partial Differential Equations by the Finite Element Method. Cambridge University press, Cambridge.

Johnson, P.C., Jackson, R., 1987. Frictional–Collisional constitutive relations for granular materials with application to plane shearing. J. Fluid Mech. 176, 67–93.

Kuipers, J.A.M., van Duin, K.J., van Beckum, F.P.H., van Swaaij, W.P.M., 1992a. A numerical model of gas-fluidized beds. Chemical Engineering Science 47, 1913–1924.

Kuipers, J.A.M., Prins, W., van Swaaij, W.P.M., 1992b. Numerical calculation of wall to bed heat transfer coefficients in gas-fluidised beds. AIChE Journal 38, 1079–1091.

Ma, D., Ahmadi, G., 1986. An equation of state for dense rigid sphere gases. J. Chem. Phys. 84, 3449–3450.

Lin, J.S., Chen, M.M., Chao, B.T., 1985. A novel radioactive particle tracking facility for measurement of solids motion in gas fluidized beds. AIChE Journal 31, 465–473.

Lim, K.S., Zhu, J.X., Grace, J.R., 1995. Hydrodynamics of gas–solid fluidization. Int. J. Multiphase Flow 21, 141–193.

Lyczkowski, R.W., Gamwo, I.K., Dorban, V., Ai, Y.H., Chao, B.T., Chen, M., Gidaspow, D., 1993. Validation of computed solids hydrodynamics and pressure oscillations in a bubbling atmospheric fluidized bed. Powder Technology 76, 65–77.

Lun, C.K.K., Savage, S.B., Jeffrey, D.J., Chepurniy, N., 1984. Kinetic theories for granular flow: inelastic particles in Couette flow and slightly inelastic particles in a general flow field. J. Fluid Mech. 140, 223–256.

Ocone, R., Astarita, G., 1993. A pseudo-thermodynamic theory of granular flow rheology. Journal of Rheology 37, 727–742.

Pain, C.C., Mansoorzadeh, S., de Oliveira, C.R.E., Goddard, A.J.H., 1998. Numerical modelling of gas–solid fluidized beds using the two-fluid approach. Int. J. Numer Meth. Fluids, submitted.

Qin, S., Liu, D., 1982. Application of optical fibers to measurement and display of fluidized systems. In: Kwauk, M., Kunii, D. (Eds.), Fluidization 82: Science and Technology. Science Press, Beijing, pp. 258–266.

Roy, R., Davidson, J.F., Tuponogov, V.G., 1990. The velocity of sound in fluidised beds. Chem. Eng. 45, 3233–3245.

Samuelsberg, A., Hjertager, B.H., 1996. An experimental and numerical study of flow patterns in a circulating fluidized bed reactor. Int. J. Multiphase Flow 22, 575–591.

Savage, S.B., 1983. Granular flows at high shear rates. In: Meyer, R.E. (Ed.), Theory of Dispersed Multiphase Flow. Academic Press, New York, p. 339.

Schlichting, H., Kestin, J., 1968. Boundary-Layer Theory, 6th ed. McGraw-Hill, New York.

Shahinpoor, M., Ahmadi, G., 1983. A kinetic theory for the rapid flow of rough identical spherical particles and the evolution of fluctuation. In: Shahinpoor, M. (Ed.), Advances in Mechanics and the Flow of Granular Materials, vol. II. Trans. Tech. Pub, Andermannsdorf, Switzerland, p. 641.

Soo, S.L., 1967. Fluid Dynamics of Multiphase Systems. Blaisdell Press, New York.

Sun, B., Gidaspow, D., 1999. Computation of circulating fluidized-bed riser flow for the fluidization VIII benchmark test. Ind. Eng. Chem. Res. 38, 787–792.

Thonglimp, V., 1981. Docteur-Ingenieur thesis. Institut National Polytechnique, Toulouse.

Toei, R., Matsuno, R., Tejima, T., 1967. The coalescence of bubbles in the gas–solid fluidized bed. Kagaku Kogaku 31, 1238–1239.

Tsuji, Y., Kawaguchi, T., 1993. Discrete particle simulation of two dimensional fluidized bed. Powder Technology 77, 79–87.

van der Hagen, T.H.J.J., van Dam, H., Harteveld, W., Hoogenboom, J.W., Khotylev, V.A., Mudde, R.F., 1999. Studies on the inhomogeneous core density of fluidized bed nuclear reactor, to be published.

Wolf, A., Swift, J.B., Swinney, H.L., Vastano, J.A., 1985. Determining Lyapunov exponents from a time series. Physica. 16D, 285–317.